REVIEW
SPACE PHYSICS: MAGNETOSPHERIC PHYSICS

Earth and Planetary Physics
7: 109–118, 2023
doi: 10.26464/epp2023009

Dynamics of the inner electron radiation belt: A review

YuXuan Li, Chao Yue*, Ying Liu, Qiu-Gang Zong, Hong Zou, and YuGuang Ye

Institute of Space Physics and Applied Technology, Peking University, Beijing 100871, China

Key Points:

- Using advanced measurements by the Van Allen Probes, inner electron radiation belt structures are investigated.
- Recent advances of inner radiation belt acceleration and loss mechanisms are summarized and discussed.
- Questions for future inner radiation belt analysis are summarized.

Citation: Li, Y. X., Yue, C., Liu, Y., Zong, Q.-G., Zou, H., and Ye, Y. G. (2023). Dynamics of the inner electron radiation belt: A review. *Earth Planet. Phys.*, *7*(1), 109–118. http://doi.org/10.26464/epp2023009

Abstract: The Van Allen radiation belts are an extraordinary science discovery in the Earth magnetosphere and consist of two electron belts. The inner Van Allen belt contains electrons of 10s to 100s keV; the outer belt consists mainly of 0.1−10 MeV electrons. Their dynamics have been analyzed for decades. The newly-launched Van Allen Probes provide unprecedented opportunities to investigate the inner belt more thoroughly. Data from this advanced mission have allowed scientists to demonstrate that the inner belt was formed not only through inward transport of outer belt electrons but Cosmic Ray Albedo Neutron Decay (CRAND) has also played an important role. In addition, the inner belt electrons show energy-dependent variations and present "zebra stripe" structures in the energy spectrum. At the same time, scientists have further confirmed that the electrons in the inner radiation belt get lost through coulomb collision and wave-particle interaction. Despite these advances, important questions remain unanswered and require further investigation. The launch of Macau Science Satellite-1 mission, with its low inclination angle and low altitude orbit, will provide advanced radiation belt data for better understanding of the structure and dynamics of the inner electron radiation belt.

Keywords: Macau Scientific Satellite-1 mission; zebra stripes; inward transport; CRAND; coulomb collision; wave-particle interaction

1. Introduction

The Van Allen radiation belt, since its discovery in 1958 (Van Allen et al., 1958) through the abnormal Geiger counter observation onboard Explorer 1, has been a fundamental topic in inner magnetosphere research. Figure 1 shows the model that has been accepted since the mid-1960s: two-belts of energetic particles. The outer belt, consisting mainly of 0.1−10 MeV electrons, is located between the 3–7 *L* shell regions (*L*-shell is a parameter, in units of planetary radius, that describes distances from the center of planet at which magnetic fields cross the planet's magnetic equator). The inner belt lies between 1.1 to 2.5 *L* shell, and contains 10−100 MeV protons and 10s to 100s keV electrons. The slot region between the two belts is caused by the pitch angle (the angle between the direction of particle velocity and magnetic field vector) scattering loss through wave-particle interactions (Lyons and Thorne, 1973). This model represents general Van Allen Belt features during geomagnetic quiet times; however, the radiation belts are very dynamic and complicated during active geomagnetic active periods (e.g., Reeves et al., 2016; Li YX et al., 2021; Bregou et al., 2022).

In general, the outer electron radiation belt is considered to vary significantly during active magnetospheric periods (e.g., Baker et al., 2013; Reeves et al., 2016; Hao YX et al., 2020), whereas the inner belt has been treated as relatively stable. The lifetime of > 1 MeV electrons in the inner belt was estimated to be roughly one year, and the < 1 MeV electrons have been thought to vary only during major geomagnetic storms (Bostrom et al., 1970). Observations and models supported this picture until the 1990s (e.g., Russell and Thorne, 1970; Lyons and Thorne, 1973).

After the launch of more advanced satellites in the near-Earth region, such as the Combined Release and Radiation Effects Satellite (CREES, Johnson and Kierein, 1992), the Solar, Anomalous, and Magnetospheric Particle Explorer (SAMPAX, Baker et al., 1993), and POLAR (Blake et al., 1995) missions in the 1990s, more data relevant to the understanding of the inner radiation belt have been obtained. Multiple peaks in the electron fluxes at a given *L* value were observed, and energetic electron injections and several different loss processes were reported (e.g., Li XL et al., 1993; Voss et al., 1998). Because of occasional contamination from the penetration of ambient inner belt protons, the electron data obtained in the inner radiation belt had some uncertainties. Recently, Claudepierre et al. (2015) developed a method to correct the background contamination from the bremsstrahlung X-rays and penetrating protons, and applied this method to the electron data provided by the more advanced Van Allen Probes (or RBSPs, Mauk et al., 2013) mission, which was launched in 2012.

Correspondence to: C. Yue, yuechao@pku.edu.cn
Received 23 JUL 2022; Accepted 24 OCT 2022.
Accepted article online 29 NOV 2022.

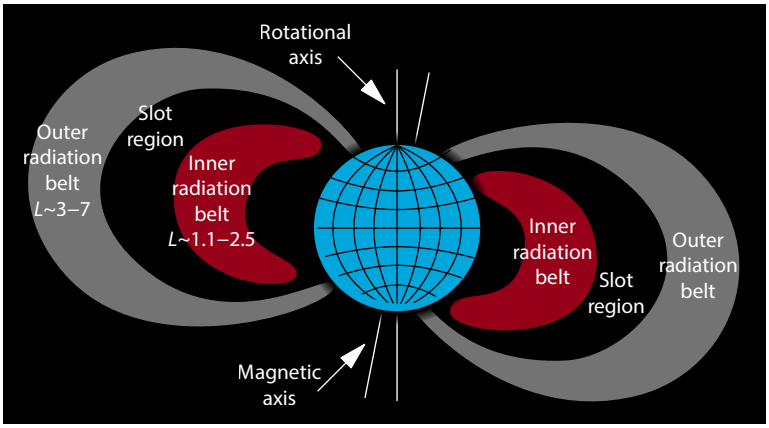

Figure 1. 2-D radiation belt model consisting of the inner and outer radiation belt. This figure is adapted from the wikipedia website (https://en.wikipedia.org/wiki/Van_Allen_radiation_belt).

With this high-fidelity electron data set, Fennell et al. (2015) showed a surprising result—that the > 1 MeV electron fluxes are in general very low with only about 0.1 $cm^{-2}s^{-1}sr^{-1}keV^{-1}$ at inner radiation belt, suggesting that most of the time the inner radiation belt does not contain many MeV electrons. The energy-dependent variations of keV electrons were found to occur more frequently than initially thought (e.g., Turner et al., 2015; Reeves et al., 2016). Figure 2 shows the time evolution of electron fluxes as a function of *L* shell and universal time during the whole year of 2013 for five different energy channels, from tens of keV to MeV (Figure 2a–2e). The solar wind speed, interplanetary magnetic field (IMF) B_z, and Disturbance Storm-Time (*Dst*) indices are also provided in Figure 2f–2h. The unit of the electron fluxes is $cm^{-2}s^{-1}sr^{-1}keV^{-1}$. As shown in Figure 2a, the fluxes of 1553 keV electrons are less than 1 $cm^{-2}s^{-1}sr^{-1}keV^{-1}$ at *L* ~2, extremely low compared with those of electrons with lower energies. Injection events of electrons with hundreds of keV into the inner radiation belt are observed during geomagnetic active times, such as in July 2013. When considering the energy spectrum of inner belt electrons, an interesting "zebra stripe" structure was revealed, based on the measurement of Van Allen Probes, and several studies analyzed in detail the formation mechanism (e.g., Ukhorskiy et al., 2014; Liu Y et al., 2016). Another important discovery was the three-belt structure (Baker et al., 2013), which is generated due to the magnetopause shadowing effect and radial diffusion driven by ultralow frequency (ULF) wave or substorm injection (e.g., Mann et al., 2016; Pinto et al., 2018; Hao YX et al., 2020).

The dynamics of the inner radiation belt have long been a hot research topic and have advanced significantly during the Van Allen Probes era. Acceleration mechanisms generally consist of the radial transport of outer belt electrons and the recently discovered Cosmic Ray Albedo Neutron Decay (CRAND); loss mechanisms generally involve coulomb scattering and wave-particle interactions (e.g., Li W and Hudson, 2019; Ripoll et al., 2020). In this review, we focus in Section 2 on the electron source of the inner radiation belt; in Section 3 we discuss formation of the "zebra stripe" structure in the inner radiation belt; the role that various waves play in the dynamics of inner belt electrons is presented in Section 4; Section 5 presents a summary and a list of open questions for future inner belt explorations.

2. The Sources of Inner Radiation Belt Electrons

The formation of the inner radiation belt is an important topic and has been widely studied. Inner radiation belt electrons could come either by transport inward from the outer radiation belt, or from local processes. CRAND is an important process to produce electrons locally in the inner radiation belt region. Neutrons originating in collisions between cosmic rays and the atmosphere decay in the magnetosphere and produce ions, electrons and antineutrinos. Measurements and models have provided data describing neutron fluxes from the atmosphere (e.g., Morris et al., 1995; Selesnick, 2015; Selesnick and Looper, 2022). Recently, Li XL et al. (2017) confirmed that, at the inner edge of the inner belt, CRAND electrons are the dominant source; their analysis is based on Colorado Student Space Weather Experiment (CSSWE) CubeSat observations. Xiang Z et al. (2019) and Zhang K et al. (2019) extended this idea and suggested that CRAND is a significant source of inner belt and slot region (*L* ~2–3) electrons during quiet magnetospheric periods. As the decay rate of neutrons is relatively constant, however, this mechanism could not explain the fast variation of inner belt electrons at more active geomagnetic times.

Radial diffusion is a traditional scenario for transport of particles to the radiation belt (e.g., Lyons and Thorne, 1973; Zhao H and Li XL, 2013). The bounce and drift averaged Fokker–Planck equation (Schulz and Lanzerotti, 1974) is one of the general models used to simulate the radial diffusion of radiation belt electrons. Brautigam and Albert (2000) derived the *Kp*-dependent diffusion coefficient associated with electrostatic (D_{LL}^{E}) or electromagnetic (D_{LL}^{B}) fluctuations in the outer belt. While Zhao H and Li XL (2013), simulating the trapped electrons in April 2010, found that the diffusion coefficients for inner belt electrons are much larger than D_{LL}^{B}, they concluded that the time scale of radial diffusion is too long to explain the fast enhancement of the electrons in the inner belt during geomagnetic active times.

Injections of electrons from the outer radiation belt are another source of radial transport. Many studies have focused on fast MeV electron injections. Li XL et al. (1993) reported a MeV electron flux enhancement event at *L* ~2.5 associated with strong electromagnetic field oscillations observed by the CREES satellite after storm sudden commencement on March 24, 1991. They concluded that

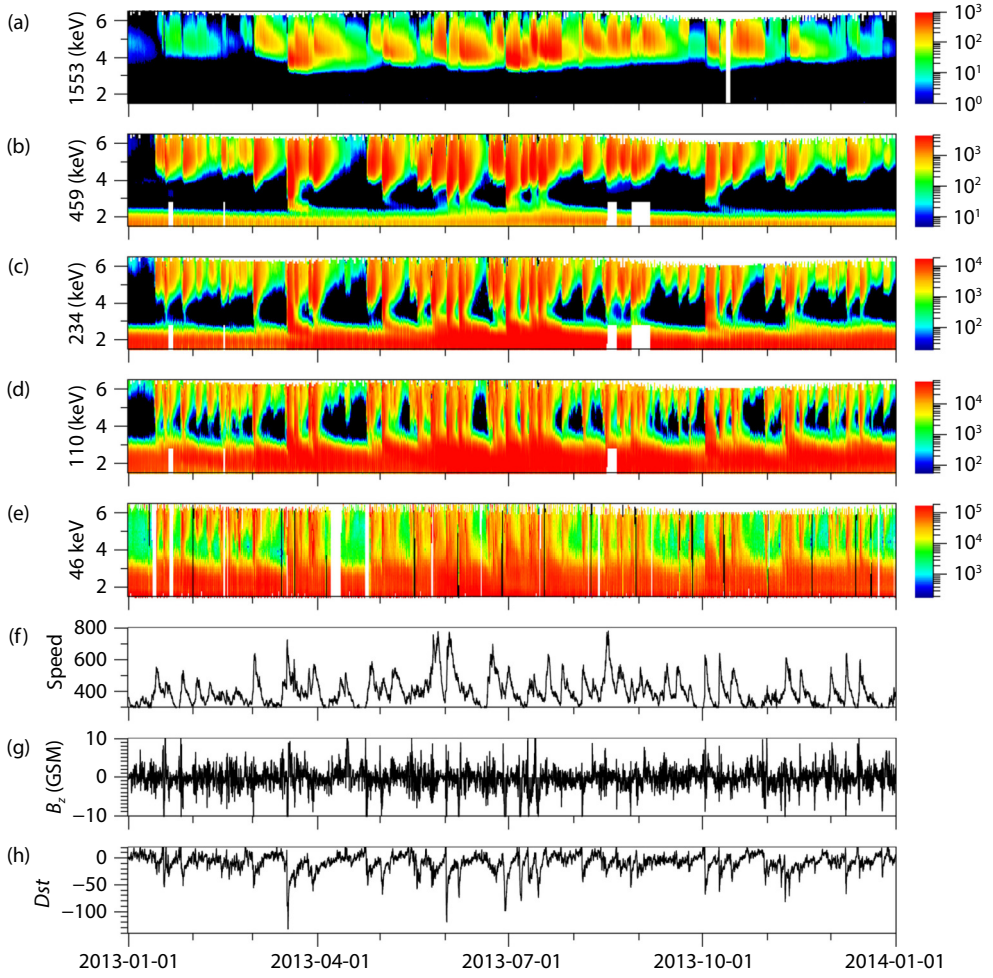

Figure 2. Electron fluxes as a function of *L* shell and time for multi-energy electrons from the Van Allen Probes mission for 2013. (a–d) Background-corrected MagEIS electron fluxes, (e) electron fluxes from HOPE, and (f–h) solar wind speed, IMF B_z, and *Dst* indices. Electrons of different energies behave differently in different events. MagEIS = Magnetic Electron–Ion Spectrometer; HOPE = Helium, Oxygen, Proton, and Electron Mass Spectrometer; IMF = interplanetary magnetic field. This figure is adopted from Reeves et al. (2016).

the injected electrons were accelerated adiabatically by the storm's electromagnetic field perturbations. Claudepierre et al. (2017) also reported a case of MeV electron enhancement in the inner belt from background-corrected Van Allen Probe data in April 2015. This enhancement of MeV electrons occurs when the magnetosphere is significantly affected by a strong storm, and this population could last for several months to a year due to its small loss rate. This acceleration process should be the same as the results presented in Li XL et al. (1993). Furthermore, Kim et al. (2021) reported rapid injection of MeV electrons associated with strong substorm depolarization at $L > 3.8$. The enhancements occurred almost simultaneously for 10s keV to multi-MeV electrons, with the lowest *L* of enhancement region located farther out for higher energy.

On the other hand, fast injections of keV electrons are more frequently observed and widely analyzed. Turner et al. (2015) studied deep injections at *L* shells ≤ 4 (minimum at 2.5) associated with substorms and distinguished them from higher *L* shell injections. They suggested that the injections result from electrons interacting with a fast magnetosonic wave in the Pi2 frequency range inside the plasmasphere. The enhanced convection and penetration of electric fields may also account for electron injections. Su YJ et al. (2016) simulated and reproduced the March 2013 injection of 200–500 keV electrons with six electric field models, although the details of non-diffusive electron transport relied significantly on the choice of the electric field model.

Local acceleration is another way in which inner radiation belt electrons can be created. Zhao H et al. (2014) presented a peculiar butterfly pitch angle distribution of ~460 keV electrons and suggested that the butterfly distributions are generated by acceleration of inter-median pitch angles (~60°) through fast magnetosonic waves. Zhang ZX et al. (2021) recently reported a weak enhancement of hundreds of keV electrons at *L* ~1.5–2 during storm time, based on observations from the Zhangheng-1 satellite (Shen XH et al., 2018) and Van Allen Probes, and concluded that the weak electron acceleration is due to interaction with the magnetosonic waves.

Turner et al. (2017) systematically analyzed sudden particle enhancements at low *L* shells (SPELLS) events of ~50 keV–1 MeV electrons; SPELLS events include both fast injections and fast local accelerations. They suggest that sudden particle enhancements

during geomagnetic active conditions are the dominant source of inner radiation belt electrons in the hundreds of keV range. Figure 3 shows the time evolution of phase space density (PSD) as a function of L^* (a parameter similar to L shell, but considering the non-dipole component and conservation of the third adiabatic invariant—see Roederer, 1970) for three fixed magnetic moments (M) and the second adiabatic invariant (K) before, during, and after the SPELLS event. The color from blue to yellow represents the time evolution as labeled in Figure 3a. It is shown that the PSD of different M and K all increased dramatically during SPELLS event for $L^* > 3$. Turner et al. (2017) suggest that the responsible mechanism could simply be enhanced convection; they ruled out the possibility of local acceleration through nonadiabatic wave-particle interaction as there was no local peak in the PSD functions. However, no clear mechanism of the fast transport that drives the SPELLS events has been determined, so future work is needed on this topic.

3. "Zebra Stripe" Structure in the Inner Radiation Belt

A peculiar feature in the energy spectrum of inner belt electrons, named "zebra stripe", was reported by Ukhorskiy et al. (2014). Figure 4 shows a typical case of the "zebra stripe" structure, presented in Liu Y et al. (2016). Panels from top to bottom in Figure 4 correspond to continuous measurements by the Van Allen Probe B. The left column shows the measured electron fluxes as a function of energies and L shells; the middle column displays the detrended electron fluxes as a function of L shells and electron drift frequency; the right column demonstrates the detrended electron fluxes as a function of electron drift frequency at given L shells, along with fitted results. The detrended fluxes are the difference between the original logarithmic electron fluxes and the average of the logarithmic electron fluxes of a moving window of nine-energy-channels at every specific L shell (or every time point) to illustrate the characteristics of the "zebra stripe" patterns. As demonstrated in the Energy-L spectrum (left column), the fluxes of keV to MeV electrons display one or multiple peaks at a given L value, with valleys between the peaks. Imhof and Smith (1966) first revealed such characteristics in electron energy-L spectrum, in which only one peak was identified (in 1.3 MeV electrons). Later on, Imhof et al. (1981) reported a multi-peak structure of 68–1152 keV electrons, detected by the P78-1 satellite. Thereafter more cases were reported through observations from low-earth orbit satellites (e.g., Sauvaud et al., 2013) and middle-earth orbit satellites (e.g., Ukhorskiy et al., 2014; Liu Y et al., 2016).

The most distinctive characteristic of the "zebra stripes" is that the peaks or valleys of the fluxes correspond to particles with generally constant drift periods over a broad range of L shells, and the frequency intervals are the same. Another feature is that the number of stripes increases in consecutive observations, and the frequency interval corresponding to the peak or valley is reduced. These two features are clearly illustrated in the first and second columns of Figure 4. These characteristics were first interpreted as resonances of particles with magnetic fluctuations close to the drift periods (e.g., Cladis, 1966; Pinto et al., 1991). Sauvaud et al. (2013) suggested, based on ground measurements, that the formation of "zebra stripes" is due to particles resonating with ultralow frequency (ULF) waves during active geomagnetic conditions. However, Ukhorskiy et al. (2014) found that the "zebra stripes" are ubiquitous in both quiet and active geomagnetic conditions. They argued further that ULF waves could not explain all of the "zebra stripes" because ULF waves are not a long-lasting phenomenon and do not have a discrete structure. Further analysis combining statistical observational results with simulations has shown that the zebra stripes could originate from the periodic drift of electrons in a global electric field. The peaks reflect electrons with different drift frequencies corresponding to different numbers of drift orbits around the earth. Ukhorskiy et al. (2014) reproduced the stripes through a test-particle model with a global monochromatic azimuthal electric field, which was driven by the

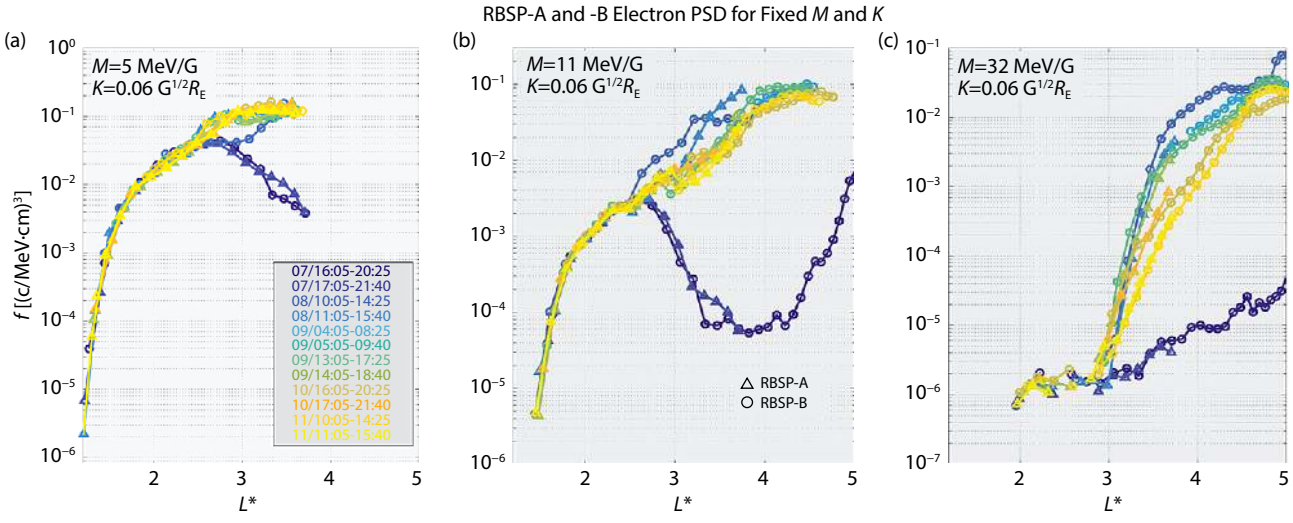

Figure 3. Evolution of electron phase space density as a function of L^* for electrons of different magnetic moments—before, during, and after the SPELLS event on 07 June 2015. The PSDs of electrons whose moments were 5, 11, and 32 MeV/G are shown in the left, middle, and right plots. Triangle markers represent data from RBSP A, while circle markers represent data from RBSP B. Different colors show data from different orbit tracks of the satellite. This figure is adopted from Turner et al. (2017).

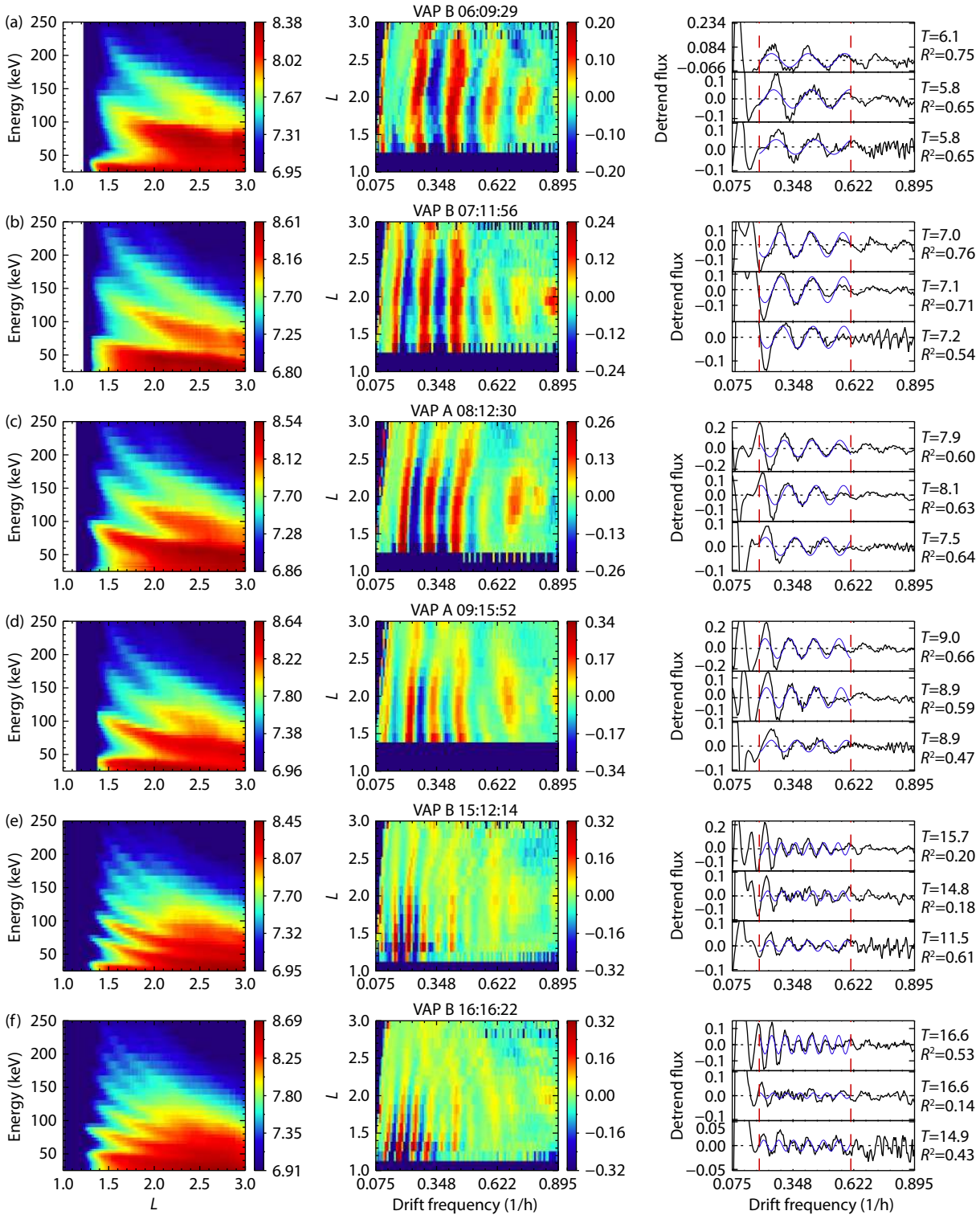

Figure 4. Continuous electron spectrograms observed by RBSPs on 16 February 2014. Left column: Energy–*L* spectrogram of energetic electrons. Middle column: *L*-drift frequency spectrogram of detrended logarithmic energetic electrons. Right column: Detrended logarithmic fluxes (black lines) and fitted detrended logarithmic fluxes (blue lines) in three *L* shell regions (1.5–2.0, 2.0–2.5, and 2.5–3.0), respectively. This Figure is adopted from Liu Y et al. (2016).

diurnal oscillations of the corotational electric field. Liu Y et al. (2016) performed a test-particle simulation with a more generalized azimuthal electric field model that could represent both static electric fields and transient electric fields. They revealed that static convection and transient electric fields could also produce zebra stripes. They found that the temporal evolution of the stripes was linearly correlated with the observational time, which resulted in a decrease in the drift frequency separations. In contrast, Lejosne and Roederer (2016) considered that the zebra strips result purely from particle drift velocity modulation by F

region zonal plasma drifts.

The electric field measurement in the plasmasphere is still a challenge; the mechanism that generates the electric field and zebra stripes has not been fully determined at this point. Lejosne and Mozer (2020a) developed a method to determine the onset of zebra structure based on a Van Allen Probe database by analyzing the formation of zebra stripes statistically. They found that the occurrence of zebra stripes is closely related to substorm activities. The peaks in the zebra stripes are created preferentially in the morning sector, while the valleys in the zebra stripes are created preferentially in the pre-midnight sector. This result suggested that the trapped particle drift motion is perturbed by the prompt penetrated electric field associated with substorms: the electrons in the dawn–morning sector move inward to generate the peaks in the spectrum, and the electrons in the dusk-to-pre-midnight sector move outward to generate the spectrum's valleys. Quantification of radial movement from the measured amplitude of the zebra stripes is still under investigation (e.g., Lejosne et al., 2022).

In addition, inversed zebra stripes are also observed. Figure 5 shows an event with inversed stripes in the energy–L spectrum. Panel (a) shows the initial electron fluxes as a function of energy and L shell; Panel (b) shows the smoothed fluxes (calculated in the same way as Liu Y et al., 2016); Panel (c) shows the detrended fluxes calculated by subtracting the smoothed fluxes from the initial fluxes; Panel (d) shows the detrended fluxes as a function of magnetic angular drift velocity and L shell. Note in Panel (d) that electrons with the same drift frequencies exhibit opposite characteristics in higher L shells (L > 2.6) and lower L shells (L < 2.6). Lejosne and Mozer (2020b) suggested that a decrease in radial flux profile, instead of a variation of electric field direction, causes such inversion. However, such cases are relatively rare (~300 inversed cases compared with ~2000 normal cases).

4. Interactions Between Inner Belt Electrons and Plasma Waves

The two principal decay processes are coulomb collision and wave-particle interactions. In low L shells (L < 1.5), radiation belt electrons collide with ambient neutrals in the upper atmosphere. Through elastic and inelastic collisions, the electrons diffuse into the loss cone and scatter into the atmosphere (e.g., Walt and Farley, 1978; Selesnick, 2012). However, at relatively higher altitudes, wave-particle interactions become the dominant processes.

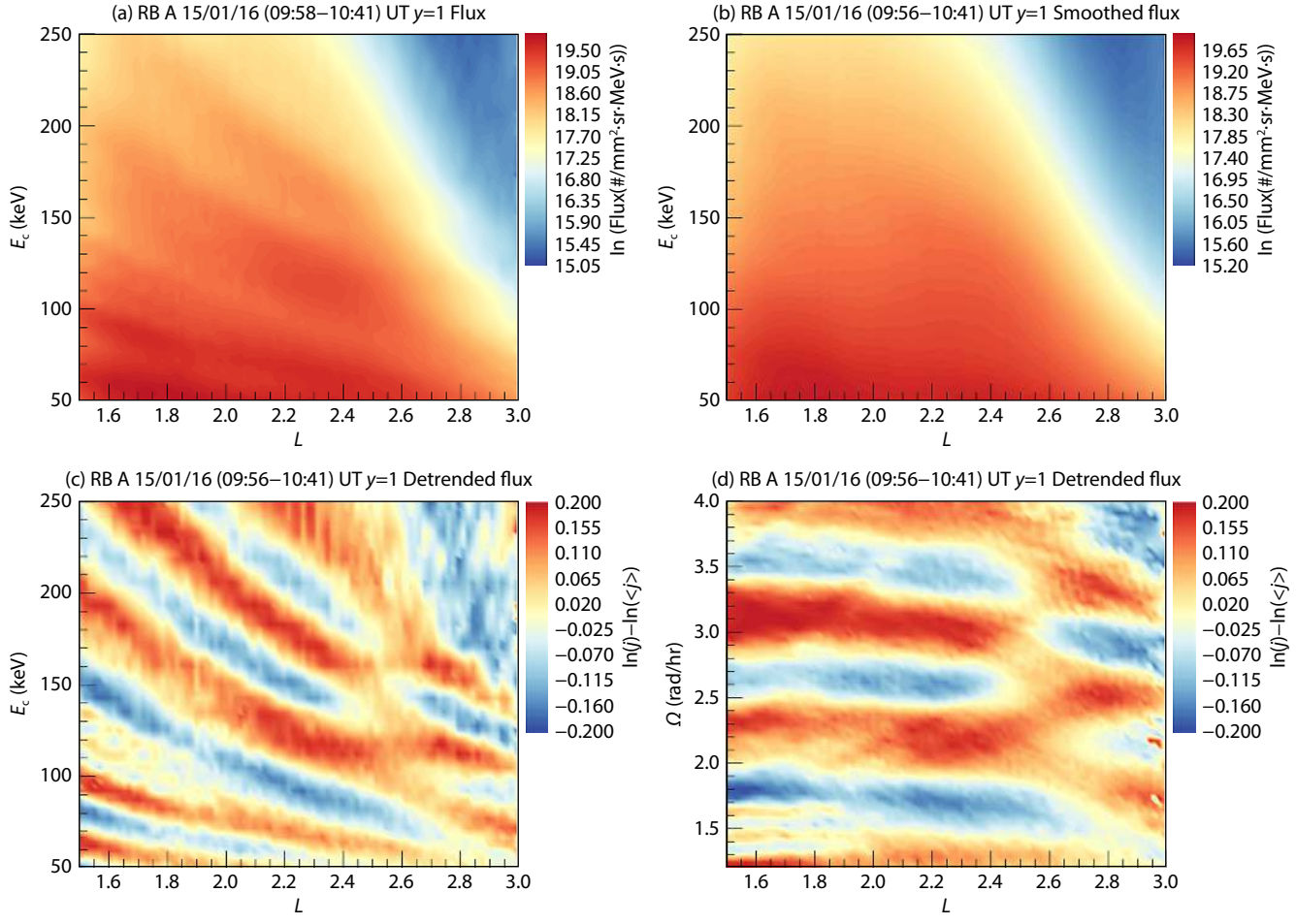

Figure 5. 90° pitch angle differential electron fluxes from Van Allen Probes A on 16 January 2015 between 09:56 and 10:41 UT. (a) The measured fluxes, (b) the smoothed fluxes, and (c) the detrended fluxes, as a function of kinetic energy and L. Panel (d) presents the detrended fluxes, as a function of the magnetic angular drift velocity. The peaks and valleys are more apparent in Panels (c) and (d) than in Panel (a) and inverse around L = 2.6. This figure is adopted from Lejosne and Mozer (2020b).

Waves in the inner radiation belt region generally consist of natural and artificial waves. The main natural waves are the magnetosonic wave, lightning-generated whistler wave, and hiss wave. Emission from ground-based very-low-frequency (VLF) transmitters can penetrate into the ionosphere and propagate to the $L < 3$ region, forming the artificial portion of plasma waves. Natural waves are generally much stronger than artificial waves, but both effects could be significant (e.g., Li W et al., 2015; Ma QL et al., 2016; Meredith et al., 2019; Green et al., 2020). The magnetosonic wave may accelerate electrons, as discussed in Section 2; the three other types of waves will scatter and cause loss of radiation belt electrons. Observations and simulations have demonstrated the decay of radiation belt electrons due to various plasma waves (e.g., Abel and Thorne, 1998; Li W et al., 2015; Green et al., 2020; Hua M et al., 2020).

Figure 6 shows the lifetime of 500 keV electron as a function of L shell, calculated from theory predictions due to coulomb collision and various waves (lines), and derived from the satellite measurements (dots), respectively. The hiss and lightning-generated whistlers affect the lifetime of inner radiation belt electrons in higher L shells ($L > 2$) while the VLF transmitter may bifurcate the inner belt. In the following, we discuss different waves and their properties in the magnetosphere.

The lightning-generated whistlers (LGWs) are ~2–12 kHz waves propagating from the troposphere to the L shell where the wave frequency is close to the lower hybrid resonance frequency of the equatorial plane (e.g., Meredith et al., 2007). LGWs are usually restricted to the plasmasphere and relatively stronger in the nightside since ionospheric D-region on the dayside could weaken such waves (e.g., Helliwell, 1965; Ripoll et al., 2020). LGWs could precipitate electrons through resonance interactions (e.g., Rodger et al., 2003). Green et al. (2020) analyzed the LGW effect statistically. They suggested that LGWs are relatively important for scattering electrons from several hundred keV to several MeV at L ~1.5 and from tens of keV to ~1 MeV at L ~2.5, but have little impact on energetic electron dynamics at higher L-shells.

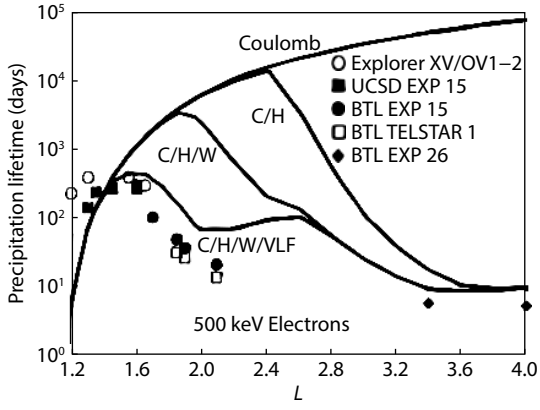

Figure 6. Precipitation lifetime of 500 keV electrons driven by scattering effect of Coulomb collisions (C), Coulomb collisions and plasmaspheric hiss (C/H), Coulomb collisions, Plasmaspheric hiss and lightning-generated whistlers (C/H/W), and by all scattering mechanisms (C/H/W/VLF). Observed decay rates are also plotted for comparison. This figure is adopted from Abel and Thorne (1998).

The whistler mode hiss waves are broad-band (~50 Hz–10 kHz) structureless right-handed polarized whistler mode waves typically observed in the high-density region, i.e., the plasmasphere and plume (e.g., Li W et al., 2015; Nakamura et al., 2018). The origin of hiss wave is under debate, from either local generation or inward propagation from chorus waves (e.g., Bortnik et al., 2009; Yue C et al., 2017; Fu HB et al., 2021). Hiss waves are responsible for the precipitation at the outer plasmasphere of electrons of tens to hundreds keV and also play a critical role in forming the slot region and S-shape energy spectrum of electrons (e.g., Reeves et al., 2016). In the inner radiation belt region, the intense lower frequency (< 600 Hz) hiss waves appear mostly in the dayside high-L region ($L > 1.3$), while the intense higher frequency ($\gtrsim$600 Hz) hiss waves appear mostly in the low-L region ($L < 1.3$), both dayside and nightside (e.g., Wang JZ et al., 2020; Yang L et al., 2022). In these regions, the hiss wave tends to interact with higher energy electrons, whereas its effect on electron precipitation is relatively insignificant (Li W et al., 2015).

The VLF transmitter waves are narrow band waves of 10–30 kHz (e.g., Hua M et al., 2020). As shown in Figure 6, interaction between the electrons and the VLF transmitter waves could significantly reduce electron lifetime at L ~2 for 500 keV electrons. Several concurrent ground and satellite observations of VLF transmitter waves and electron precipitations indicate that the VLF transmitter waves play an important role in electron loss (e.g., Graf et al., 2009; Wang YL et al., 2018). Electron precipitation by the VLF transmitter waves is caused primarily by the first-order cyclotron resonance (Sauvaud et al., 2008). An interesting feature generated by the VLF transmitter wave-driven precipitation is bifurcation of the inner electron belt, which is frequently observed. Claudepierre et al. (2020) reported an energy-dependent local electron flux minimum at L ~2 based on observations from Van Allen Probes. Hua M et al. (2020) compared the simulation results of electron PSD evolution with and without VLF transmitter waves. They demonstrated the primary role that VLF transmitters played in electron flux bifurcation. Recently, rocket exhaust driven amplification (REDA) of VLF transmitter waves has successfully amplified the wave power by 20–30 dB (Bernhardt et al., 2021). In simulation, such a strong wave could accelerate ~300 keV electrons at L ~2.5 (Hua M et al., 2022). Future observations will be needed to test this mechanism.

The fast magnetosonic waves are also whistler mode waves, generated under turbulent magnetospheric conditions mostly at dayside by ring distribution of protons (e.g., Russell et al., 1970; Ma QL et al., 2016; Yue C et al., 2020). Their frequency ranges from the local proton gyrofrequency to the lower hybrid resonance frequency (e.g., Laakso et al., 1990; Santolík et al., 2004) and propagates nearly perpendicular to the ambient geomagnetic field (Chen LJ and Thorne, 2012). This wave mode could interact with keV to MeV electrons through Landau resonance, causing acceleration of electrons whose pitch angle is 60–80 degrees and forming butterfly-shaped pitch angle distributions (e.g., Zhao H et al., 2014). The effect of this kind of wave has been discussed in Section 2.

Besides the waves mentioned above, ultralow frequency (ULF) waves, with a frequency range from 2 mHz–5 Hz, are commonly observed in the magnetosphere and can interact with charged

particles through drift resonance or drift-bounce resonance. Considering the drift and bounce periods of relativistic electrons, the ULF wave could resonate with such high energy electrons merely through drift resonance. Most studies have focused on interactions between MeV electrons and ULF waves in the outer radiation belt. For example, Li L et al. (2017) compared their modeled results of ULF wave-particle interaction with observations of several keV electron fluxes in a ULF wave field at L ~7.5. They found consistency in the gradually diagonal stripes. Hao YX et al. (2019) reported a fast acceleration of 3.4 MeV electrons by ULF wave at L ~5 during an interplanetary shock event. Few studies have considered the ULF wave effect on radiation belt electrons in the inner belt. Through multi-satellite analysis of the ULF wave, the location and timescale of its perturbations in the magnetosphere have been determined by Zhao XX et al. (2020). Future work on interactions between inner belt electrons and ULF waves would be valuable.

To summarize the plasma waves' interaction with inner radiation belt electrons, there are several wave modes, consisting mainly of lightning-generated whistlers, whistler mode hiss waves, VLF transmitter waves, and fast magnetosonic waves. They interact with inner belt electrons in different ways and/or at different regions. The first three wave modes pitch angle scatter the inner belt electrons and cause them to be lost to the atmosphere predominately at different regions: the hiss wave affects electrons at higher L shell ($L > 2.5$); the LGWs scatter electrons at lower L shell ($L < 2.5$); the VLF transmitter waves also scatter electrons at lower L shell ($L < 2.5$) and affect electrons more significantly at L ~2, which cause the bifurcation of the inner radiation belt. The fast magnetosonic waves could accelerate electrons and form butterfly-shaped pitch angle distributions of electrons. Apart from the waves mentioned above, interactions between inner belt electrons and ULF waves are also important and should be paid more attention to in the future.

5. Summary

In the Van Allen Probes era, the dynamics of the inner radiation belt are being extensively analyzed and the knowledge of the inner radiation belt is greatly advanced. The inner belt contains mainly electrons in the range of tens of keV with frequent energy-dependent variations during geomagnetic activities. The sudden flux enhancements due to inward transport provide the primary source of inner radiation belt electrons; the CRAND accounts for the electrons in the inner edge. Coulomb decay and wave-particle interactions form the structure of the inner belt and the slot region, while VLF transmitter waves may bifurcate the inner belt. Large scale electric fields appear to cause "zebra stripe" characteristics in the electron energy spectrum; the PSD of electrons may affect the shape of the stripes.

Questions also arise based on previous studies. For example, what makes the sudden flux enhancement, what drives the large-scale electric field to form "zebra stripes" and what other roles do plasma waves play in their interaction with the electrons. New qualitative and quantitative observations and advanced simulations are expected in future work. Macau University of Science and Technology is leading a Macau Science Satellite-1 mission which will be launched soon in 2023. The Macau mission consists of A and B satellites with low-inclination and low-altitude orbits. The energetic electron detector, built in our Institute of Space Physics and Applied Technology at Peking University, will provide high fidelity energetic electron data. It can measure electrons from 50 keV to ~3 MeV, and such dataset will help to elucidate physical mechanisms that drive the dynamic process of electrons in the inner radiation belt.

Acknowledgments

The study was supported by NSFC research grant 41974191, China National Space Administration project D020303, and the National Key R&D Program of China 2020YFE0202100. Figures in this review paper were not freshly plotted from data; they were adapted from published papers that are cited accordingly in the references.

References

Abel, B., and Thorne, R. M. (1998). Electron scattering loss in Earth's inner magnetosphere: 1. Dominant physical processes. *J. Geophys. Res.*: *Space Phys.*, *103*(A2), 2385–2396. https://doi.org/10.1029/97JA02919

Baker, D. N., Mason, G. M., Figueroa, O., Colon, G., Watzin, J. G., and Aleman, R. M. (1993). An overview of the Solar Anomalous, and Magnetospheric Particle Explorer (SAMPEX) mission. *IEEE Trans. Geosci. Remote Sens.*, *31*(3), 531–541. https://doi.org/10.1109/36.225519

Baker, D. N., Kanekal, S. G., Hoxie, V. C., Henderson, M. G., Li, X., Spence, H. E., Elkington, S. R., Friedel, R. H. W., Goldstein, J., … Claudepierre, S. G. (2013). A long-lived relativistic electron storage ring embedded in Earth's outer Van Allen belt. *Science*, *340*(6129), 186–190. https://doi.org/10.1126/science.1233518

Bernhardt, P. A., Bougas, W. C., Griffin, M. K., Watson, C., Langley, R. B., Howarth, A. D., James, H. G., Siefring, C. L., Perry, G. W., … Gołkowski, M. (2021). Strong amplification of ELF/VLF signals in space using neutral gas injections from a satellite rocket engine. *Radio Sci.*, *56*(2), e2020RS007207. https://doi.org/10.1029/2020RS007207

Blake, J. B., Fennell, J. F., Friesen, L. M., Johnson, B. M., Kolasinski, W. A., Mabry, D. J., Osborn, J. V., Penzin, S. H., Schnauss, E. R., … Hall, D. (1995). CEPPAD. *Space Sci. Rev.*, *71*(1-4), 531–562. https://doi.org/10.1007/BF00751340

Bortnik, J., Li, W., Thome, R. M., Angelopoulos, V., Cully, C., Bonnell, J., Le Contel, O., and Roux, A. (2009). An observation linking the origin of plasmaspheric hiss to discrete chorus emissions. *Science*, *324*(5928), 775–778. https://doi.org/10.1126/science.1171273

Bostrom, C. O., Beall, D. S., and Armstrong, J. C. (1970). Time history of the inner radiation zone, October 1963 to December 1968. *J. Geophys. Res.*, *75*(7), 1246–1256. https://doi.org/10.1029/JA075i007p01246

Brautigam, D. H., and Albert, J. M. (2000). Radial diffusion analysis of outer radiation belt electrons during the October 9, 1990, magnetic storm. *J. Geophys. Res.*: *Space Phys.*, *105*(A1), 291–309. https://doi.org/10.1029/1999JA900344

Bregou, E. J., Hudson, M. K., Kress, B. T., Qin, M. R., and Selesnick, R. S. (2022). Gleissberg cycle dependence of inner zone proton flux. *Space Wea.*, *20*(7), e2022SW003072. https://doi.org/10.1029/2022SW003072

Chen, L. J., and Thorne, R. M. (2012). Perpendicular propagation of magnetosonic waves. *Geophys. Res. Lett.*, *39*(14), L14102. https://doi.org/10.1029/2012GL052485

Cladis, J. B. (1966). Resonance acceleration of particles in the inner radiation belt. In B. M. McCormac (Ed.), *Radiation Trapped in the Earth's Magnetic Field* (pp. 112-115). Bergen, Norway: Springer. https://doi.org/10.1007/978-94-010-3553-8_9

Claudepierre, S. G., O'Brien, T. P., Blake, J. B., Fennell, J. F., Roeder, J. L., Clemmons, J. H., Looper, M. D., Mazur, J. E., Mulligan, T. M., … Larsen, B. A. (2015). A background correction algorithm for Van Allen Probes MagEIS electron flux measurements. *J. Geophys. Res.*: *Space Physics*, *120*, 5703–5727. https://doi.org/10.1002/2015JA021171

Claudepierre, S. G., O'Brien, T. P., Fennell, J. F., Blake, J. B., Clemmons, J. H.,

Looper, M. D., Mazur, J. E., Roeder, J. L., Turner, D. L., … Spence, H. E. (2017). The hidden dynamics of relativistic electrons (0.7-1.5 MeV) in the inner zone and slot region. *J. Geophys. Res.*: *Space Phys.*, *122*(3), 3127–3144. https://doi.org/10.1002/2016JA023719

Claudepierre, S. G., Ma, Q., Bortnik, J., O'Brien, T. P., Fennell, J. F., and Blake, J. B. (2020). Empirically estimated electron lifetimes in the Earth's radiation belts: Comparison with theory. *Geophys. Res. Lett.*, *47*(3), e2019GL086056. https://doi.org/10.1029/2019GL086056

Fennell, J. F., Claudepierre, S. G., Blake, J. B., O'Brien, T. P., Clemmons, J. H., Baker, D. N., Spence, H. E., and Reeves, G. D. (2015). Van Allen Probes show that the inner radiation zone contains no MeV electrons: ECT/MagEIS data. *Geophys. Res. Lett.*, *42*(5), 1283–1289. https://doi.org/10.1002/2014GL062874

Fu, H. B., Yue, C., Ma, Q. L., Kang, N., Bortnik, J., Zong, Q. G., and Zhou, X. Z. (2021). Frequency-dependent responses of plasmaspheric hiss to the impact of an interplanetary shock. *Geophys. Res. Lett.*, *48*(20), e2021GL094810. https://doi.org/10.1029/2021GL094810

Graf, K. L., Inan, U. S., Piddyachiy, D., Kulkarni, P., Parrot, M., and Sauvaud, J. A. (2009). DEMETER observations of transmitter-induced precipitation of inner radiation belt electrons. *J. Geophys. Res.*: *Space Phys.*, *114*(A7), A07205. https://doi.org/10.1029/2008JA013949

Green, A., Li, W., Ma, Q., Shen, X. C., Bortnik, J., and Hospodarsky, G. B. (2020). Properties of lightning generated whistlers based on Van Allen Probes observations and their global effects on radiation belt electron loss. *Geophys. Res. Lett.*, *47*(17), e2020GL089584. https://doi.org/10.1029/2020GL089584

Hao, Y. X., Zong, Q. G., Zhou, X. Z., Rankin, R., Chen, X. R., Liu, Y., Fu, S. Y., Baker, D. N., Spence, H. E., … Claudepierre, S. G. (2019). Global-scale ULF waves associated with SSC accelerate magnetospheric ultrarelativistic electrons. *J. Geophys. Res.*: *Space Phys.*, *124*(3), 1525–1538. https://doi.org/10.1029/2018JA026134

Hao, Y. X., Zong, Q. G., Zhou, X. Z., Zou, H., Rankin, R., Sun, Y. X., Chen, X. R., Liu, Y., Fu, S. Y., … Claudepierre, S. G. (2020). A short-lived three-belt structure for sub-MeV electrons in the Van Allen belts: Time scale and energy dependence. *J. Geophys. Res.*: *Space Phys.*, *125*(9), e2020JA028031. https://doi.org/10.1029/2020JA028031

Helliwell, R. A. (1965). *Whistlers and Related Ionospheric Phenomena*. Mineola, New York: Dover Publications.

Hua, M., Li, W., Ni, B. B., Ma, Q. L., Green, A., Shen, X. C., Claudepierre, S. G., Bortnik, J., Gu, X. D., … Reeves, G. D. (2020). Very-low-frequency transmitters bifurcate energetic electron belt in near-Earth space. *Nat. Commun.*, *11*, 4847. https://doi.org/10.1038/s41467-020-18545-y

Hua, M., Bortnik, J., Ma, Q. L., and Bernhardt, P. A. (2022). Radiation belt electron acceleration driven by Very-Low-Frequency transmitter waves in near-Earth space. *Geophys. Res. Lett.*, *49*(10), e2022GL099258. https://doi.org/10.1029/2022GL099258

Imhof, W. L., and Smith, R. V. (1966). Low altitude measurements of trapped electrons. In B. M. McCormac (Ed.), *Radiation Trapped in the Earth's Magnetic Field* (pp. 100-111). Bergen, Norway: Springer. https://doi.org/10.1007/978-94-010-3553-8_8

Imhof, W. L., Gaines, E. E., and Reagan, J. B. (1981). High-resolution spectral features observed in the inner radiation belt trapped electron population. *J. Geophys. Res.*: *Space Phys.*, *86*(A4), 2341–2347. https://doi.org/10.1029/JA086iA04p02341

Johnson, M. H., and Kierein, J. (1992). Combined release and radiation effects satellite (CRRES): Spacecraft and mission. *J. Spacecraft Rockets*, *29*(4), 556–563. https://doi.org/10.2514/3.55641

Kim, H. J., Lee, D. Y., Wolf, R., Bortnik, J., Kim, K. C., Lyons, L., Choe, W., Noh, S. J., Choi, K. E., … Li, J. (2021). Rapid injections of MeV electrons and extremely fast step-like outer radiation belt enhancements. *Geophys. Res. Lett.*, *48*(9), e2021GL093151. https://doi.org/10.1029/2021GL093151

Laakso, H., Junginger, H., Roux, A., Schmidt, R., and de Villedary, C. (1990). Magnetosonic waves above $f_c(H^+)$ at geostationary orbit: GEOS 2 results. *J. Geophys. Res.*: *Space Phys.*, *95*(A7), 10609–10621. https://doi.org/10.1029/JA095iA07p10609

Lejosne, S., and Roederer, J. G. (2016). The "zebra stripes": An effect of *F* region zonal plasma drifts on the longitudinal distribution of radiation belt particles. *J. Geophys. Res.*: *Space Phys.*, *121*(1), 507–518. https://doi.org/10.1002/2015JA021925

Lejosne, S., and Mozer, F. S. (2020a). Experimental determination of the conditions associated with "zebra stripe" pattern generation in the Earth's inner radiation belt and slot region. *J. Geophys. Res.*: *Space Phys.*, *125*(7), e2020JA027889. https://doi.org/10.1029/2020JA027889

Lejosne, S., and Mozer, F. S. (2020b). Inversion of the energetic electron "zebra stripe" pattern present in the Earth's inner belt and slot region: First observations and interpretation. *Geophys. Res. Lett.*, *47*(13), e2020GL088564. https://doi.org/10.1029/2020GL088564

Lejosne, S., Fejer, B. G., Maruyama, N., and Scherliess, L. (2022). Radial transport of energetic electrons as determined from the "zebra stripes" measured in the Earth's inner belt and slot region. *Front. Astron. Space Sci.*, *9*, 823695. https://doi.org/10.3389/fspas.2022.823695

Li, L., Zhou, X. Z., Zong, Q. G., Rankin, R., Zou, H., Liu, Y., Chen, X. R., and Hao, Y. X. (2017). Charged particle behavior in localized ultralow frequency waves: Theory and observations. *Geophys. Res. Lett.*, *44*(12), 5900–5908. https://doi.org/10.1002/2017GL073392

Li, W., Ma, Q., Thorne, R. M., Bortnik, J., Kletzing, C. A., Kurth, W. S., Hospodarsky, G. B., and Nishimura, Y. (2015). Statistical properties of plasmaspheric hiss derived from Van Allen Probes data and their effects on radiation belt electron dynamics. *J. Geophys. Res.*: *Space Phys.*, *120*(5), 3393–3405. https://doi.org/10.1002/2015JA021048

Li, W., and Hudson, M. K. (2019). Earth's Van Allen radiation belts: From discovery to the Van Allen Probes era. *J. Geophys. Res.*: *Space Phys.*, *124*(11), 8319–8351. https://doi.org/10.1029/2018JA025940

Li, X. L., Roth, I., Temerin, M., Wygant, J. R., Hudson, M. K., and Blake, J. B. (1993). Simulation of the prompt energization and transport of radiation belt particles during the March 24, 1991 SSC. *Geophys. Res. Lett.*, *20*(22), 2423–2426. https://doi.org/10.1029/93GL02701

Li, X. L., Selesnick, R., Schiller, Q., Zhang, K., Zhao, H., Baker, D. N., and Temerin, M. A. (2017). Measurement of electrons from albedo neutron decay and neutron density in near-Earth space. *Nature*, *552*(7685), 382–385. https://doi.org/10.1038/nature24642

Li, Y. X., Yue, C., Hao, Y. X., Zong, Q. G., Zhou, X. Z., Fu, S. Y., Chen, X. R., and Zhao, X. X. (2021). The characteristics of three-belt structure of sub-MeV electrons in the radiation belts. *J. Geophys. Res.*: *Space Phys.*, *126*(7), e2021JA029385. https://doi.org/10.1029/2021JA029385

Liu, Y., Zong, Q. G., Zhou, X. Z., Foster, J. C., and Rankin, R. (2016). Structure and evolution of electron "zebra stripes" in the inner radiation belt. *J. Geophys. Res.*: *Space Phys.*, *121*(5), 4145–4157. https://doi.org/10.1002/2015JA022077

Lyons, L. R., and Thorne, R. M. (1973). Equilibrium structure of radiation belt electrons. *J. Geophys. Res.*, *78*(13), 2142–2149. https://doi.org/10.1029/JA078i013p02142

Ma, Q. L., Li, W., Thorne, R. M., Bortnik, J., Kletzing, C. A., Kurth, W. S., and Hospodarsky, G. B. (2016). Electron scattering by magnetosonic waves in the inner magnetosphere. *J. Geophys. Res.*: *Space Phys.*, *121*(1), 274–285. https://doi.org/10.1002/2015JA021992

Mann, I. R., Ozeke, L. G., Murphy, K. R., Claudepierre, S. G., Turner, D. L., Baker, D. N., Rae, I. J., Kale, A., Milling, D. K., … Honary, F. (2016). Explaining the dynamics of the ultra-relativistic third Van Allen radiation belt. *Nat. Phys.*, *12*(10), 978–983. https://doi.org/10.1038/nphys3799

Mauk, B. H., Fox, N. J., Kanekal, S. G., Kessel, R. L., Sibeck, D. G., and Ukhorskiy, A. (2013). Science objectives and rationale for the radiation belt storm probes mission. *Space Sci. Rev.*, *179*(1), 3–27. https://doi.org/10.1007/s11214-012-9908-y

Meredith, N. P., Horne, R. B., Glauert, S. A., and Anderson, R. R. (2007). Slot region electron loss timescales due to plasmaspheric hiss and lightning-generated whistlers. *J. Geophys. Res.*: *Space Phys.*, *112*(A8), A08214. https://doi.org/10.1029/2007JA012413

Meredith, N. P., Horne, R. B., Clilverd, M. A., and Ross, J. P. J. (2019). An investigation of VLF transmitter wave power in the inner radiation belt and slot region. *J. Geophys. Res.*: *Space Phys.*, *124*(7), 5246–5259. https://doi.org/10.1029/2019JA026715

Morris, D. J., Aarts, H., Bennett, K., Lockwood, J. A., McConnell, M. L., Ryan, J. M., Schönfelder, V., Steinle, H., and Peng, X. (1995). Neutron measurements in near-Earth orbit with COMPTEL. *J. Geophys. Res.*: *Space Phys.*, *100*(A7), 12243–12249. https://doi.org/10.1029/95JA00475

Nakamura, S., Omura, Y., and Summers, D. (2018). Fine structure of whistler mode hiss in plasmaspheric plumes observed by the Van Allen Probes. *J. Geophys. Res.: Space Phys.*, *123*(11), 9055–9064. https://doi.org/10.1029/2018JA025803

Pinto, O. Jr., Pinto, I. R. C. A., Gonzalez, W. D., and Gonzalez, A. L. C. (1991). About the origin of peaks in the spectrum of inner belt electrons. *J. Geophys. Res.: Space Phys.*, *96*(A2), 1857–1860. https://doi.org/10.1029/90JA02383

Pinto, V. A., Bortnik, J., Moya, P. S., Lyons, L. R., Sibeck, D. G., Kanekal, S. G., Spence, H. E., and Baker, D. N. (2018). Characteristics, occurrence, and decay rates of remnant belts associated with three-belt events in the Earth's radiation belts. *Geophys. Res. Lett.*, *45*(22), 12099–12107. https://doi.org/10.1029/2018GL080274

Reeves, G. D., Friedel, R. H. W., Larsen, B. A., Skoug, R. M., Funsten, H. O., Claudepierre, S. G., Fennell, J. F., Turner, D. L., Denton, M. H., … Baker, D. N. (2016). Energy-dependent dynamics of keV to MeV electrons in the inner zone, outer zone, and slot regions. *J. Geophys. Res.: Space Phys.*, *121*(1), 397–412. https://doi.org/10.1002/2015JA021569

Ripoll, J. F., Claudepierre, S. G., Ukhorskiy, A. Y., Colpitts, C., Li, X., Fennell, J. F., and Crabtree, C. (2020). Particle dynamics in the Earth's radiation belts: Review of current research and open questions. *J. Geophys. Res.: Space Phys.*, *125*(5), e2019JA026735. https://doi.org/10.1029/2019JA026735

Rodger, C. J., Clilverd, M. A., and McCormick, R. J. (2003). Significance of lightning-generated whistlers to inner radiation belt electron lifetimes. *J. Geophys. Res.: Space Phys.*, *108*(A12), 1462. https://doi.org/10.1029/2003JA009906

Roederer, J. G. (1970). *Dynamics of Geomagnetically Trapped Radiation*. Berlin, Heidelberg, Springer–Verlag. https://doi.org/10.1007/978-3-642-49300-3

Russell, C. T., and Thorne, R. M. (1970). On the structure of the inner magnetosphere. *Cosmic Electrodyn.*, *1*, 67–89.

Russell, C. T., Holzer, R. E., and Smith, E. J. (1970). OGO 3 observations of ELF noise in the magnetosphere: 2. The nature of the equatorial noise. *J. Geophys. Res.*, *75*(4), 755–768. https://doi.org/10.1029/JA075i004p00755

Santolík, O., Němec, F., Gereová, K., Macúšová, E., de Conchy, Y., and Cornilleau-Wehrlin, N. (2004). Systematic analysis of equatorial noise below the lower hybrid frequency. *Ann. Geophys.*, *22*(7), 2587–2595. https://doi.org/10.5194/angeo-22-2587-2004

Sauvaud, J. A., Maggiolo, R., Jacquey, C., Parrot, M., Berthelier, J. J., Gamble, R. J., and Rodger, C. J. (2008). Radiation belt electron precipitation due to VLF transmitters: Satellite observations. *Geophys. Res. Lett.*, *35*(9), L09101. https://doi.org/10.1029/2008GL033194

Sauvaud, J. A., Walt, M., Delcourt, D., Benoist, C., Penou, E., Chen, Y., and Russell, C. T. (2013). Inner radiation belt particle acceleration and energy structuring by drift resonance with ULF waves during geomagnetic storms. *J. Geophys. Res.: Space Phys.*, *118*(4), 1723–1736. https://doi.org/10.1002/jgra.50125

Schulz, M., and Lanzerotti, L. J. (1974). Particle diffusion in the radiation belts. In *Physics and Chemistry in Space (Vol. 7)*. Berlin, Heidelberg: Springer. https://doi.org/10.1007/978-3-642-65675-0

Selesnick, R. S. (2012). Atmospheric scattering and decay of inner radiation belt electrons. *J. Geophys. Res.: Space Phys.*, *117*(A8), A08218. https://doi.org/10.1029/2012JA017793

Selesnick, R. S. (2015). High-energy radiation belt electrons from CRAND. *J. Geophys. Res.: Space Phys.*, *120*(4), 2912–2917. https://doi.org/10.1002/2014JA020963

Selesnick, R. S., and Looper, M. D. (2022). Modeling the albedo neutron decay source of radiation belt electrons and protons. *J. Geophys. Res.: Space Phys.*, *127*(7), e2022JA030405. https://doi.org/10.1029/2022JA030405

Shen, X. H., Zhang, X. M., Yuan, S. G., Wang, L. W., Cao, J. B., Huang, J. P., Zhu, X. H., Piergiorgio, P., and Dai, J. P. (2018). The state-of-the-art of the China Seismo-Electromagnetic Satellite mission. *Sci. China Technol. Sci.*, *61*(5), 634–642. https://doi.org/10.1007/s11431-018-9242-0

Su, Y. J., Selesnick, R. S., and Blake, J. B. (2016). Formation of the inner electron radiation belt by enhanced large-scale electric fields. *J. Geophys. Res.: Space Phys.*, *121*(9), 8508–8522. https://doi.org/10.1002/2016JA022881

Turner, D. L., Claudepierre, S. G., Fennell, J. F., O'Brien, T. P., Blake, J. B., Lemon, C., Gkioulidou, M., Takahashi, K., Reeves, G. D., … Angelopoulos, V. (2015). Energetic electron injections deep into the inner magnetosphere associated with substorm activity. *Geophys. Res. Lett.*, *42*(7), 2079–2087. https://doi.org/10.1002/2015GL063225

Turner, D. L., O'Brien, T. P., Fennell, J. F., Claudepierre, S. G., Blake, J. B., Jaynes, A. N., Baker, D. N., Kanekal, S., Gkioulidou, M., … Reeves, G. D. (2017). Investigating the source of near-relativistic and relativistic electrons in Earth's inner radiation belt. *J. Geophys. Res.: Space Phys.*, *122*(1), 695–710. https://doi.org/10.1002/2016JA023600

Ukhorskiy, A. Y., Sitnov, M. I., Mitchell, D. G., Takahashi, K., Lanzerotti, L. J., and Mauk, B. H. (2014). Rotationally driven 'zebra stripes' in Earth's inner radiation belt. *Nature*, *507*(7492), 338–340. https://doi.org/10.1038/nature13046

Van Allen, J. A., Ludwig, G. H., Ray, E. C., and McIlwain, C. E. (1958). Observation of high intensity radiation by satellites 1958 Alpha and Gamma. *J. Jet Propul.*, *28*(9), 588–592. https://doi.org/10.2514/8.7396

Voss, H. D., Walt, M., Imhof, W. L., Mobilia, J., and Inan, U. S. (1998). Satellite observations of lightning-induced electron precipitation. *J. Geophys. Res.: Space Phys.*, *103*(A6), 11725–11744. https://doi.org/10.1029/97JA02878

Walt, Martin., and Farley, T. A. (1978). The physical mechanisms of the inner Van Allen belt. In *The Earth: 1-The Upper Atmosphere*. (A78-45322 20-46) New York and London, Gordon and Breach, Science Publishers, 1978, p. 303–412.

Wang, J. Z., Zhu, Q., Gu, X. D., Fu, S., Guo, J. G., Zhang, X. X., Yi, J., Guo, Y. J., Ni, B. B., and Xiang, Z. (2020). An empirical model of the global distribution of plasmaspheric hiss based on Van Allen Probes EMFISIS measurements. *Earth Planet. Phys.*, *4*(3), 246–265. https://doi.org/10.26464/epp2020034

Wang, Y. L., Zhang, X. M., and Shen, X. H. (2018). A study on the energetic electron precipitation observed by CSES. *Earth Planet. Phys.*, *2*(6), 538–547. https://doi.org/10.26464/epp2018052

Xiang, Z., Li, X. L., Selesnick, R., Temerin, M. A., Ni, B. B., Zhao, H., Zhang, K., and Khoo, L. Y. (2019). Modeling the quasi-trapped electron fluxes from cosmic ray albedo neutron decay (CRAND). *Geophys. Res. Lett.*, *46*(4), 1919–1928. https://doi.org/10.1029/2018GL081730

Yang, L., Li, L. Y., Cao, J. B., and Yu, J. (2022). Statistical properties of whistler-mode hiss waves in the inner radiation belt. *J. Geophys. Res.: Space Phys.*, *127*(5), e2022JA030444. https://doi.org/10.1029/2022JA030444

Yue, C., Chen, L. J., Bortnik, J., Ma, Q. L., Thorne, R. M., Angelopoulos, V., Li, J. X., An, X., Zhou, C., … Spence, H. E. (2017). The characteristic response of whistler mode waves to interplanetary shocks. *J. Geophys. Res.: Space Phys.*, *122*(10), 10047–10057. https://doi.org/10.1002/2017JA024574

Yue, C., Ma, Q. L., Jun, C. W., Bortnik, J., Zong, Q. G., Zhou, X. Z., Jang, E., Reeves, G. D., Spence, H. E., and Wygant, J. R. (2020). The modulation of plasma and waves by background electron density irregularities in the inner magnetosphere. *Geophys. Res. Lett.*, *47*(15), e2020GL088855. https://doi.org/10.1029/2020GL088855

Zhang, K., Li, X., Zhao, H., Schiller, Q., Khoo, L. Y., Xiang, Z., Selesnick, R., Temerin, M. A., and Sauvaud, J. A. (2019). Cosmic Ray Albedo Neutron Decay (CRAND) as a source of inner belt electrons: Energy spectrum study. *Geophys. Res. Lett.*, *46*(2), 544–552. https://doi.org/10.1029/2018GL080887

Zhang, Z. X., Xiang, Z., Wang, Y. F., Ni, B. B., and Li, X. Q. (2021). Electron acceleration by magnetosonic waves in the deep inner belt (L = 1.5-2) region during geomagnetic storm of August 2018. *J. Geophys. Res.: Space Phys.*, *126*(12), e2021JA029797. https://doi.org/10.1029/2021JA029797

Zhao, H., and Li, X. L. (2013). Modeling energetic electron penetration into the slot region and inner radiation belt. *J. Geophys. Res.: Space Phys.*, *118*(11), 6936–6945. https://doi.org/10.1002/2013JA019240

Zhao, H., Li, X., Blake, J. B., Fennell, J. F., Claudepierre, S. G., Baker, D. N., Jaynes, A. N., Malaspina, D. M., and Kanekal, S. G. (2014). Peculiar pitch angle distribution of relativistic electrons in the inner radiation belt and slot region. *Geophys. Res. Lett.*, *41*(7), 2250–2257. https://doi.org/10.1002/2014GL059725

Zhao, X. X., Hao, Y. X., Zong, Q. G., Zhou, X. Z., Yue, C., Chen, X. R., Liu, Y., Blake, J. B., Claudepierre, S. G., and Reeves, G. D. (2020). Origin of electron boomerang stripes: Localized ULF wave-particle interactions. *Geophys. Res. Lett.*, *47*(17), e2020GL087960. https://doi.org/10.1029/2020GL087960